Nano-structural stiffness measure for soft biomaterials of heterogeneous elasticity

Shu-Wen W Chen, Jean-Marie Teulon, Harinderbir Kaur, Christian Godon, Jean-Luc Pellequer

Nanoscale Horizons

ROYAL SOCIETY OF CHEMISTRY

COMMUNICATION

Cite this: *Nanoscale Horiz.*, 2023, 8, 75

Received 17th August 2022,
Accepted 21st October 2022

DOI: 10.1039/d2nh00390b

rsc.li/nanoscale-horizons

Nano-structural stiffness measure for soft biomaterials of heterogeneous elasticity†

Shu-wen W. Chen, *[ab] Jean-Marie Teulon,[a] Harinderbir Kaur,[a] Christian Godon[c] and Jean-Luc Pellequer *[a]

Measuring the structural stiffness aims to reveal the impact of nanostructured components or various physiological circumstances on the elastic response of material to an external indentation. With a pyramidal tip at a nano-scale, we employed the atomic force microscopy (AFM) to indent the surfaces of two compositions of polyacrylamide gels with different softness and seedling roots of *Arabidopsis thaliana*. We found that the stiffness–depth curve derived from the measured force exhibits a heterogeneous character in elasticity. According to the tendency of stiffness–depth curve, we decomposed the responding force into depth-impact (F_C), Hookean (F_H) and tip-shape (F_S) components, called trimechanic, where F_S and its gradient should be offset at the surface or subsurfaces of the indented material. Thereby, trimechnic theory allows us to observe how the three restoring nanomechanics change with varied depth. Their strengths are represented by the respective spring constants (k_C, k_H, k_S) of three parallel-connected spring (3PCS) analogs to differentiate restoring nanomechansims of indented materials. The effective Young's modulus $\hat{E}$ and the total stiffness k_T (= k_H + k_S) globally unambiguously distinguish the softness between the two gel categories. Data fluctuations were observed in the elasticity parameters of individual samples, reflecting nanostructural variations in the gel matrix. Similar tendencies were found in the results from growing plant roots, though the data fluctuations are expectedly much more dramatic. The zone-wise representation of stiffness by the trimechanic-3PCS framework demonstrates a stiffness measure that reflects beneath nanostructures encountered by deepened depth. The trimechanic-3PCS framework can apply any mechanical model of power-law based force–depth relationship and is compatible with thin layer corrections. It provides a new paradigm for analyzing restoring nanomechanics of soft biomaterials in response to indenting forces.

New concepts

"New concept brought by this research is the trimechanic theory, the very concept of composite nanomechanics underlying the restoring mechanism of material under an external compression. It provides a disentanglement of the linear and tip-shape related mechanical responses at various indentation depth. The novel aspects of this research are (1) define the never explored application criteria for the Sneddon's model to the study of depth-heterogeneous elasticity. (2) Design a three parallel-connected spring (3PCS) analogy for quantifying the strengths of responding nanomechanics, allowing us to differentiate circumstances exhibiting the same stiffness yet with different restoring nanomechanisms. (3) Calculate the force–derived stiffness curve as the key element for analysis instead of the force values themselves, thereby the slope of stiffness curve essentially represents the intrinsic elasticity of the material. The trimechanic theory applies to all contact-based mechanical models with a power law force–depth relationship. The prospect of this research includes a standardization of the application of stiffness measure beyond model systems toward live or clinical tissues. Particularly, stiffness measure will not stay on a stage of global assessment but goes further to link elastic behaviors with substructure of the nanomaterial."

Introduction

Recently, mechanobiology has attracted a great deal of attention on how external forces can regulate the function of proteins, cells, and tissues.[1,2] In particular, it remains elusive on how cells transduce mechanical stresses, ranging from Pascals to mega Pascals, into physiological processes and end up with serious physiopathological consequences.[3] Many attempts have been made to accurately characterize elastic properties of these soft biomaterials, including micropipette aspiration,[4] optical tweezers,[5] deformability cytometry,[6] Brillouin microscopy,[7] and the most adopted strategy, atomic force microscopy (AFM).[8] AFM indentation results have brought to evidence that certain diseases are subject to abnormal cellular mechanics, for example, a

[a] *Université Grenoble Alpes, CEA, CNRS, IBS, F-38000 Grenoble, France. E-mail: cmft551@yahoo.com, jean-luc.pellequer@ibs.fr*
[b] *Rue Cyprien Jullin, Vinay, 38470, France*
[c] *Aix Marseille University, CEA, CNRS, BIAM, 13108 Saint Paul-Lez-Durance, Cadarache, France*
† Electronic supplementary information (ESI) available. See DOI: https://doi.org/10.1039/d2nh00390b

lowered stiffness measured for cancer cells compared to normal ones.[9] Similar results were found in extracellular matrix[10,11] and tissues during cancer progression.[12,13]

In the instrumental setup of AFM for indentation, the tip attached beneath the micro-sized cantilever plays as an indenter to compress the surface of cells or tissues. In this process, cantilever deflections are recorded as the so-called force–displacement data,[14,15] from which the Young's modulus is deduced.[16] In assessment of the Young's modulus, Hertzian[17] and Sneddon's models[18] are widely used to analyze the force–depth data acquired by AFM. The latter delineates the relation between the responding force of material and the indented depth, which depends on the shape of AFM tip. Hence, various shapes of tip have been exploited to study the tip-shape effect on the magnitude of Young's modulus.[19,20] Both Hertz and Sneddon models are restricted to sample systems of linear (homogeneous) elasticity with an infinite thickness (occupying the whole half space), and the employment of an axisymmetric punch to indent the material surface normally.[21,22] The Hertz model, used for spherical probes, has some other constrains such as the indented depth must be within 10% of the sample thickness,[23] relatively small compared to the spherical radius, and without adhesive interactions and frictions between the sample and the indenter upon contacting.[22] These limitations have been attenuated by the so-called bottom-effect correction for spherical tips[24] and conical tips;[25] or using a thin layer correction[26] that has been applied to two lipid layers.[21] The case of adhesion has been tackled by JKR[27] and DMT[28] models using spherical tips.

The architecture of cells and tissues is by essence complex and non-homogeneous.[29,30] The deformation of nano-structured component caused by external stresses depends on the bonding network and strengths of its chemical groups. Such a complication in stiffness measure brought by structural complexity makes conventional models difficult in interpretation of measured stiffness, especially in the study of soft biomaterials.[31] Moreover, the substratum may impact the stiffening behaviors.[21,32] It has been reported that stiffness difference can be detected from layered samples (separate elastic bodies) with different elasticity.[33–35] Therefore, a full analysis over the entire indentation trajectory is needed for our understanding on the above-mentioned issues.

Here, we propose a robust strategy, coined trimechanic theory, to encompass elastic behaviors of soft- and bio-materials in various circumstances. The change in elastic behaviors implicates the change in the context of the material. Trimechanic theory allows us to quantify the difference of elastic responses through different combinations of three nanomechanical actions governed, respectively, by a constant, a linear and a non-linear forces.

In this article, we illustrate the concept and application of the trimechanic theory to the force–depth measurements from AFM indentation. Besides the pyramidal tip used in this work, trimechanic theory will be shown to accommodate Hertz and other Sneddon's force–depth relations for spherical tips as well.

Methodology

A. Theory and model

A.1. Indentation force and stiffness. Consider the depth and force measurements by AFM indentation as a sequence of time events, $Z(t)$ and $F_T(t)$. In practice of AFM indentation, the data acquisition is carried out in a duration of T with an time interval Δt. $\{(Z(t), F_T(t))\}$ can be re-expressed as $\{(Z_i, F_{T,i})\}$, the enumeration index i indicates the data recorded at $t = (i-1)\cdot\Delta t$. This data series can be characterized by one single Young's modulus if the study material is a homogeneously elastic body. In the use of an axisymmetric tip with smooth surfaces, the Sneddon's solutions to Boussinesq's problem[36] relates the force F_T as a quadratic function of penetrated depth Z.[18] In this work, we employed a tip of pyramidal shape, of which the force–depth relation is given elsewhere;[19] omitting i, it is written as

$$F_T = \hat{E}\frac{\tan\alpha}{\sqrt{2}}Z^2 \tag{1}$$

where $\hat{E} = E/(1-\eta^2)$, denoted as the effective Young's modulus with E the Young's modulus and η the Poisson's ratio, and α corresponds to the face angle of the squared pyramidal tip. According to eqn (1), the stiffness $F'_T \equiv \partial F_T/\partial Z$ is explicitly a linear function of penetrated depth Z with a proportional constant R_S, thus

$$F'_T = R_S Z = (\sqrt{2}\hat{E}\tan\alpha)Z. \tag{2}$$

R_S can be conceived as stiffness slope, scoring the increment of stiffness per indented depth responded by the material, and directly linked to the effective Young's modulus $\hat{E}$.

For a material of homogeneous elasticity, the stiffness curve derived from F_T should be one single linear segment with one R_S or $\hat{E}$ based on the force–depth relationship. Thereby, we exploited this property to explore elastic heterogeneity of material by examining the slope of stiffness–depth curve during an indenting process. The change in R_S reflects a change in $\hat{E}$ as well as the restoring nanomechanics of material. From eqn (1) and (2), F_T and F'_T are both zero at $Z = 0$—initial boundary conditions for applying the Sneddon's model.

A.2. Trimechanic theory for general elastic response. For a material whose elastic properties vary with indented depth, we assume they exhibit a zone-wise pattern with a cone-like shape of the indenting tip. Within each depth-zone, the data points share similar elastic properties. Explicitly, the restoring force F_T at the total depth D can be expressed as a sequence of force segments:

$$\begin{aligned} F_T(D) &= \sum_{i=1}^{m}\int_{Z_{i-1}}^{Z_i} F'_T\mathrm{d}Z = F_T(Z_{j-1}) \\ &\quad + \sum_{i=j}^{m}\int_{Z_{i-1}}^{Z_i} F'_T\mathrm{d}Z = F_T(Z_{m-1}) + \int_{Z_{m-1}}^{D} F'_T\mathrm{d}Z \end{aligned} \tag{3}$$

The limits of integration define a zone-wise region of indented depth; by default, $F_T(Z_0 = 0)$ is zero. For each indented depth-zone, say Zone j, the F_T (*cf.* the second equality of eqn (3)) can be

expressed as a composite of three force components:

$$F_T(Z) = F_T(Z_{j-1}) + F'_T(Z_{j-1}) \times (Z - Z_{j-1}) + \int_{Z_{j-1}}^{Z} [F'_T(y) - F'_T(Z_{j-1})]\,dy \quad (4)$$

The first component is the force measured at the sub-surface of the zone, Z_{j-1}; it is a constant thus denoted by F_C. In effect, F_C represents the hitherto force against the indenting tip. The second component is a Hookean force, called F_H, with a proportional constant of $F'_T(Z_j - 1)$. Removing F_C and F_H from the total force F_T, the remaining force satisfies the initial boundary conditions for applying the Sneddon's model. We denote this force as F_S to attribute it to the tip shape, from which the magnitude of $\hat{E}$ is deduced. The three force components govern three nanomechanics modes—this is trimechanic theory. Trimechanic theory is the very concept of composite nanomechanics underlying the restoring mechanism of material in the indentation trajectory. Various elastic responses are expressed as a linear combination of the three basis nanomechanics, whose strengths quantify the difference in the elastic behaviors.

A.3. The three parallel-connected spring (3PCS) analogy. To quantify the strengths of the three basis nanomechanics in an elastic response, we designated a device with three parallel-connected spring (3PCS) analogs whose elastic actions represent the three different mechanical modes; see Fig. 1. The strength of each nanomechanical response is represented by the spring constant of the corresponding spring analog.

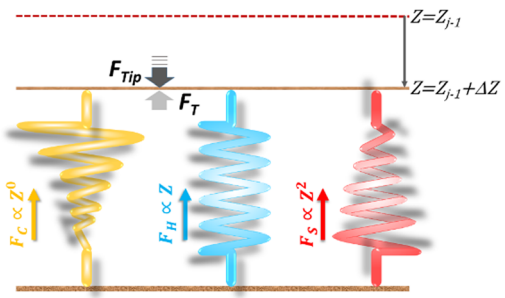

Fig. 1 Analogy of three parallel-connected springs: the elastic response (F_T) of a material to an applied force (F_{Tip}) is a composite action of three nanomechanics, respectively governed by F_C, F_H and F_S, which compose F_T. In the schematic diagram, the tip has arrived at the sub-surface of Zone j in the indentation trajectory, Z_{j-1}, and continues to indent the material with an additional compression, ΔZ. During the indentation from Z_{j-1} to $Z_{j-1} + \Delta Z$, the material exerts a restoring force F_T against the applied force F_{Tip} to form, microscopically, a quasi-equilibrium. Except the F_H-spring obeying the Hooke's law, the F_C-curve is a zero-power function of Z, while the nonlinear F_S function, in the diagram, has an exponent of 2 to exemplify the use of a pyramidal tip. The pseudo-stiffness function for the F_C-spring is inversely proportional to the indented depth, picturized by a spring with non-linearly shrinking width. The stiffness function of F_S-spring is proportional to Z, symbolized by a spring with linearly increasing width, and that of F_H-spring is a constant, thus represented by a spring of constant width. According to this spring analogy, $F_T = k_{3PCS} \cdot \Delta Z$, where $k_{3PCS} = k_C + k_H + k_S$, the sum of the spring constants of the three spring devices.

Among the 3PCS analogs, the F_H-spring is the only one having a typical spring constant, $k_{H,j} = F'_T(Z_j - 1)$ for zone j; it is essentially the total stiffness measured at the subsurface of the visited zone. Two other spring analogs for F_C and F_S do not have the standard spring constant, which will be represented by the average of their stiffness functions. As a constant, F_C contributes none to stiffness measure. Were there a stiffness function corresponding to F_C, it would be inversely proportional to the amount of compression to make up the force constant. Accordingly, F_C would act like a force thresholder, forbidding the tip without sufficient applied force continuing to indent the material. However, averaging such a pseudo-stiffness function cannot yield a finite number, thus we took $F_T(Z_{j-1})/\Delta Z_j$ as the spring constant of the F_C-spring, $k_{C,j}$, with $\Delta Z_j = Z_j - Z_{j-1}$.

For the F_S-spring, we averaged the corresponding stiffness function (eqn (2)) over the indented zone and obtained the spring constant:

$$k_{S,j} = R_{S,j} \cdot \Delta Z_j/2 \text{ or } \hat{E}_j \cdot \tan\alpha \cdot \Delta Z_j/\sqrt{2}. \quad (5)$$

We define $k_{T,j} = k_{H,j} + k_{S,j}$ as the stiffness measure for the indented material to represent the stiffness measure for the material indented through the depth-zone j. This zone-wise representation is based on behaviors of $F'_T - Z$ curve, to the contrary of stiffness tomography that slices the F_T–Z curve into segments (or layers for indentation depth) without care for the initial boundary conditions imposed on the nonlinear force and the contribution of Hookean nanomechanincs.[37–39] As shown, the relative strengths of Hookean and tip-shape nanomechanics, $r_{H,j}$ and $r_{S,j}$, are complementary to each other for $r_{H,j} = k_{H,j}/k_{T,j}$ and $r_{S,j} = 1 - r_{H,j}$. Taken together, an elastic response can be fully described by the trimechanic-3PCS framework in a quadruplet format: $[\Delta Z_j, k_{C,j}, k_{T,j}, r_{S,j}]$, the necessary and sufficient parameters to rebuild the fitting curves for F_T and three decomposed force components. Detailed calculations can be found in ESI.†

B. Material preparation and AFM instrumentation

B.1. The study systems of soft materials. System 1: the specimen is a 10.4% polyacrylamide gel of about 1.0 mm thickness. For this system, we used a triangular silicon nitride MLCT-BIO-DC cantilever D with nominal k = 0.03 N m^{-1}, L = 225 μm, W = 20 μm, F = 15 kHz (Bruker AFM probes, Camarillo, CA, USA), and a squared pyramid shape for the AFM tip with a nominal opening angle of 35°. The ingredient of 10.4% polyacrylamide gel includes 245 μL of acrylamide solution (40%, stored at 4 °C, Sigma-Aldrich A8887), 300 μL of Bis-acrylamide (2%, stored at 4 °C, Sigma-Aldrich 146072), 1.5 μL of tetramethylenediamine (TEMED, Euromedex, 50406) and 10 μL of ammonium persulfate (APS, 10%, Sigma-Aldrich, A3678) mixed in 443 μL of ultrapure water (MilliQ systems). The gel was assembled as reported previously[40] except that 50 μL of gel were deposited at the center of an O-ring from a polypropylene micro-tube (BRAND®, 780712) which was dipped in Sigmacote® (Sigma-Aldrich, SL2) beforehand.

System 2: the specimen is a 7.4% polyacrylamide gel of about 1.0 mm thickness. The same AFM instrumentation was used as for System 1. The 7.4% polyacrylamide gel was prepared by mixing with 176 μL of acrylamide solution, 210 μL of Bis-acrylamide, 1.5 μL of TEMED, and 10 μL of APS in 602 μL of ultrapure water. The two gel materials were made on the same day. A preparation protocol of polyacrylamide gels with tunable elastic properties can be found elsewhere.[41]

Experimental setups of AFM for System 1 and 2: we employed an AFM multimode 8 (Bruker, Santa Barbara, CA, USA) equipped with a J-scanner and nanoscope-V controller to perform indentations on gel specimen. The force–displacement measurements were acquired using the force volume mode of the Nanoscope 9.2 software, and the data were collected in a matrix fashion with 8 × 8 or 16 × 16 spots distributed over the material surface in a size of 2 × 2 μm^2, and each data curve consists of 512 data points with a ramp size smaller than 2 μm.

B.2. The study systems of live tissues. Systems 3 and 4: the specimens are a 4 day-old seedling root from *Arabidopsis thaliana* with a thickness of about 0.12 mm.[42] The sowing and growing of the plant seeds followed the procedures described elsewhere.[43] In brief, the roots were deposited on a glass covered with pressure sensitive adhesive NuSil MED1-1356 (NuSil Technology LLC, Carpinteria, CA, USA), and kept alive by covering with 200 μL growth solution (MES buffer 3.5 mM, pH 5.5–5.8 with MS liquid medium diluted to 1/10).[44] The indenter adopted for the system is the triangular pyrex silicon nitride PNP-TR cantilever #2 with nominal k = 0.08 N m^{-1}, L = 200 μm, W = 28 μm, F = 17 kHz, which holds a square pyramidal tip with an opening angle of 35° (NanoWorld, Neuchatel, Switzerland).

Experimental setups of AFM for Systems 3 and 4: the data values were acquired with a Dimension 3100 AFM (Bruker, Santa Barbara, CA, USA) equipped with a hybrid scanner and a nanoscope V controller. We recorded the data in a standard approach of force–distance measurements with the picoforce mode of the Nanoscope 7.3 software. Each data curve composed of 4096 points with a ramp size of 3 μm. All the indentation experiments on plants were performed in a single day.

Results and discussion

A. Elastic behaviors of soft materials

We present the results of AFM indentation for two gel composites with different concentrations of acrylamide and bis-acrylamide cross-linker, yet with the same molar ratio of acrylamide to bis-acrylamide, 16 : 1 (see Methodology). The gel system of higher (10.4%) concentration is presumably stiffer than that of the lower (7.4%) one. The former is thus called hard gel while the latter soft. The indentation (F_T–Z) and F_T-derived stiffness–depth (F'_T–Z) curves for the two gel systems are presented in Fig. 2. The computational tasks of generating F_T–Z and F'_T–Z curves from force–distance (F_d–z) data as well as the F_T decomposition into three components are described in the ESI.† In Fig. 2a, the F'_T–Z curves of both systems rise up

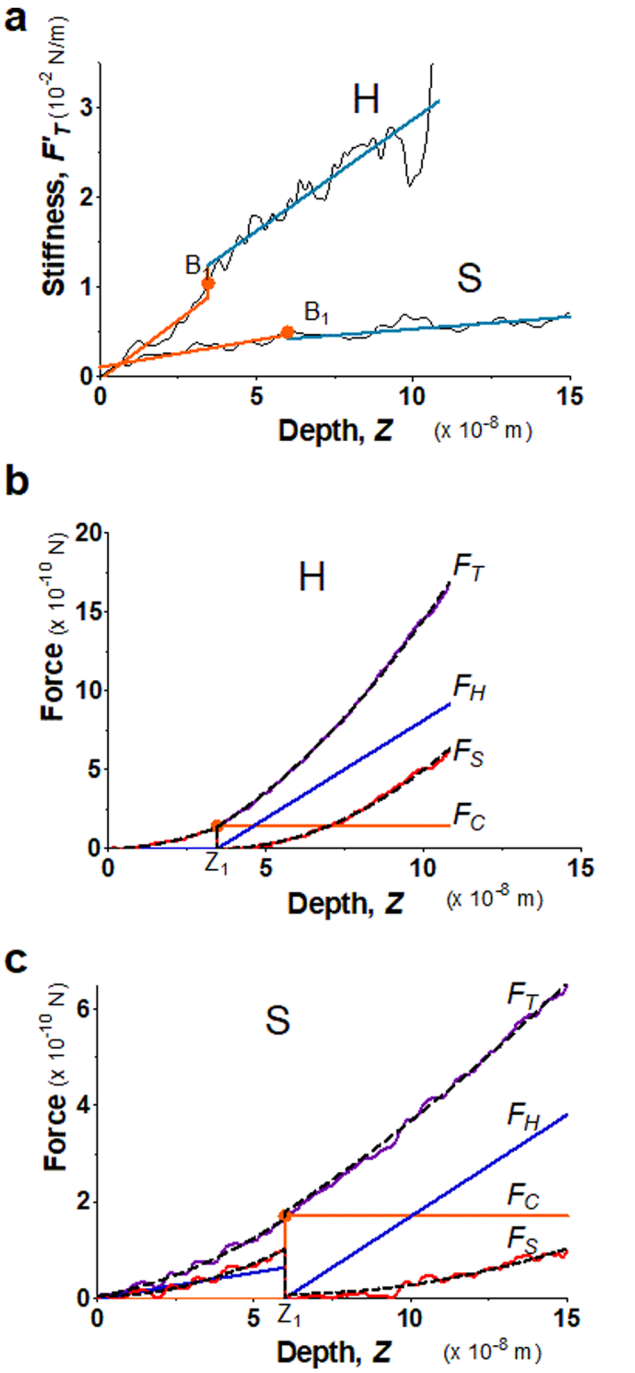

Fig. 2 Elastic behaviors of gel materials under the AFM indentation. (a) Stiffness–depth curves of two gel materials with different degrees of softness; "H" labels the hard gel while "S" labels the soft. The presenting graphs have been cut on the right for improving the clarity. In the full size, the total length of indented depth is 108 nm for the hard gel and 257.9 nm for the soft. The black solid lines present the F_T-derived stiffness data values. B_1 is the point breaking the F'_T–Z curve into two segments at a depth of Z_1. Here, Z_1 = 34.6 nm for "H" and Z_1 = 59.9 nm for "S". $\Delta Z_1 = Z_1 - Z_0 = Z_1$, $\Delta Z_2 = Z_2 - Z_1$, while Z_2 for both gels is the end of the indentation depth. Each stiffness segment was fitted to a linear function, drawn by an orange line for the first segment and in a light-blue color for the second one. (b) Decompose the restoring force of the hard gel (System 1) into three force components. F_T, F_C, F_H and F_S-curves are correspondingly presented by magenta, orange, blue and red lines, while fitting curves are drawn by black dashed lines. (c) Decompose the restoring force of the soft gel (System 2) into three force components. Similar to b, F_T, F_C, F_H and F_S are presented by magenta, orange, blue and red lines, respectively. The fitting results are drawn by black dashed lines.

with deeper indented depth. However, the one of the hard gel rises up faster and reaches a greater magnitude than that of the soft at the same depth, giving the stiffer property to the hard gel. The two curves have two linear segments with distinguished R_S values, indicating the entire indentation trajectory can be modeled as two depth-zones with different elasticity. We obtained $R_{S,1}$ = 265 and $R_{S,2}$ = 249 kPa for the hard gel. Similarly, $R_{S,1}$ = 60.5 and $R_{S,2}$ = 27.3 kPa for the soft gel. As seen later, the tendency of $\hat{E}$ would be closely related with that of R_S.

Fig. 2b and c present the curves of F_T as well as the three force components for the two gel systems. We deduced the $\hat{E}$ values from F_S-curves (Table 1) and shows that the hard gel has greater $\hat{E}$'s globally. We list the values of trimechanic-3PCS quadruplets in Table 1. We found that k_T unambiguously distinguishes the softness between soft and hard gels. As shown for this hard gel sample, the k_S dominates the total stiffness, k_T, in the first depth-zone, while k_H becomes greater than k_S at the end. Similarly, k_S is greater than k_H for the soft gel during the first depth-zone indentation while k_H is greater than to k_S in the second depth-zone.

Based on their nanomechanical types, k_H and k_S account for the resistances of material to surface displacement (non-bending action) and the extent of the surface penetrated, respectively. This behavior is illustrated by the change in r_S value, a numerical quantification for penetration ease. It is closely related to rigidity or deformability of the material. For either system, k_T steadily increases with deepened depth and accords with the tendency of $F'_T - Z$ curve. The structure of gel material formed by polymerization of acrylamide and bis-acrylamide depends on many factors such as gel concentration, molar ratio, pH and temperature.[45,46]

The k_H and k_S or r_S may provide detailed information on stiffening progresses of various indented spots of one gel or different gel composites. It is noteworthy that an effectively sharp tip should be employed instead of a large colloidal indenter for probing such a structural stiffness of material. For a nanostructured material, large spherical tips lead to a result averaged over heterogeneous elastic properties of the material. Consequently, stiffness variations attributed to different substructures and energetics on a nano-meter scale are often overlooked.

We compared the results from the trimechanic-3PCS model with the pyramid tip from AtomicJ software,[47] which aims to obtain the best fit of the indentation curve to the Sneddon's solution with a single segment by varying the location of the contact point. The fitting results of responding force from our model and AtomicJ-pyramid are shown in Fig. S2a and b (ESI†). Regarding the fitting goodness, the trimechanic-3PCS model yields a perfect fit, whereas AtomicJ-pyramid performed a poor fitting, particularly on the beginning of the indentation curve. From the data of $\hat{E}$ and k_T, it shows that the stiffness of material represented by AtomicJ-pyramid reflects an averaged value in contrast to the refined structural stiffness provided by the trimechanic-3PCS model. Moreover, the stiffness measure by trimechanic-3PCS model follows the tendency of the stiffness–depth curve accurately. It indicates that the trimechanic-3PCS model can be used to delineate the change in elasticity of the material in depth.

Table 1 The results of 3PCS quadruplet parameters for gel systems

	Hard		Soft	
Zone index	1	2	1	2
ΔZ (nm)	34.6	73.6	59.9	198
k_C (mN m^{-1})	0.00	1.92	0.00	0.86
k_T (mN m^{-1})	3.92	20.0	2.66	6.52
r_S	1.00	0.41	0.60	0.35
$\hat{E}$ (kPa)	230	236	54.4	23.4

r_s is dimensionless throughout the paper.

Beside the illustrating gel samples for the trimechanic-3PCS model shown in Fig. 2, we have applied this framework to 91 indentation curves of hard gel and 155 of soft gel; the results of k_T and $\hat{E}$ are presented in a graph format (see Fig. S3, ESI†). It shows that local elastic behaviors of these gel samples are not necessarily identical. Globally, the category of hard gel (upper sections of Fig. S3a and b, ESI†) exhibits a shorter length of indentation trajectory (the horizontal coordinate) yet much stiffer (brighter colors in intensity) than that of soft gel. It reveals that the hard gel accelerates the stiffening process shortly in depth against the deeper indentation by the AFM tip. Subsequently, the variation in the number of depth-zone is somewhat related to elasticity change in the indentation trajectory.

B. Elastic behaviors of live tissues

Biological tissues are often composed of complex structures. The probed surface of seeding roots of *A. thaliana* is formed of the external epidermal cell wall, which is structured with complex intertwining of cellulose, hemicellulose, and pectin,[48] including about 40% of water.[49] Two seedling roots (System 3 and 4) were chosen particularly for illustrating the advantages of using the trimechanic-3PCS model for analyzing elastic responses of live tissues with similar turgor pressure in a condition of constant temperature and buffer medium. In Fig. 3a, System 3 exhibits only one linear segment for the stiffness–depth curve while the other five. For the latter system, the slope of F_T-derive stiffness varies gradually and leads to a bent curve, unlike the former one that can be modeled by one straight line. These findings imply the impact of heterogeneous structure on the stiffness measure of plant root tissue, which cannot be modeled as one uniform shell structure.[50] Although System 4 has numerous depth-zones, the total depth of indentation is much shorter than that of System 3, 400 nm *vs.* ~1 μm. These depths indicate that the indentation was performed within the range of the external epidermal cell wall.[51] Fig. 3b and c show their corresponding force curves and the three force components.

In comparison with AtomicJ-pyramid (Fig. S2c and d, ESI†), we found that when the contact point and force fittings from both models are in good agreement, the deduced effective Young's moduli are unsurprisingly comparable, 45.2 and

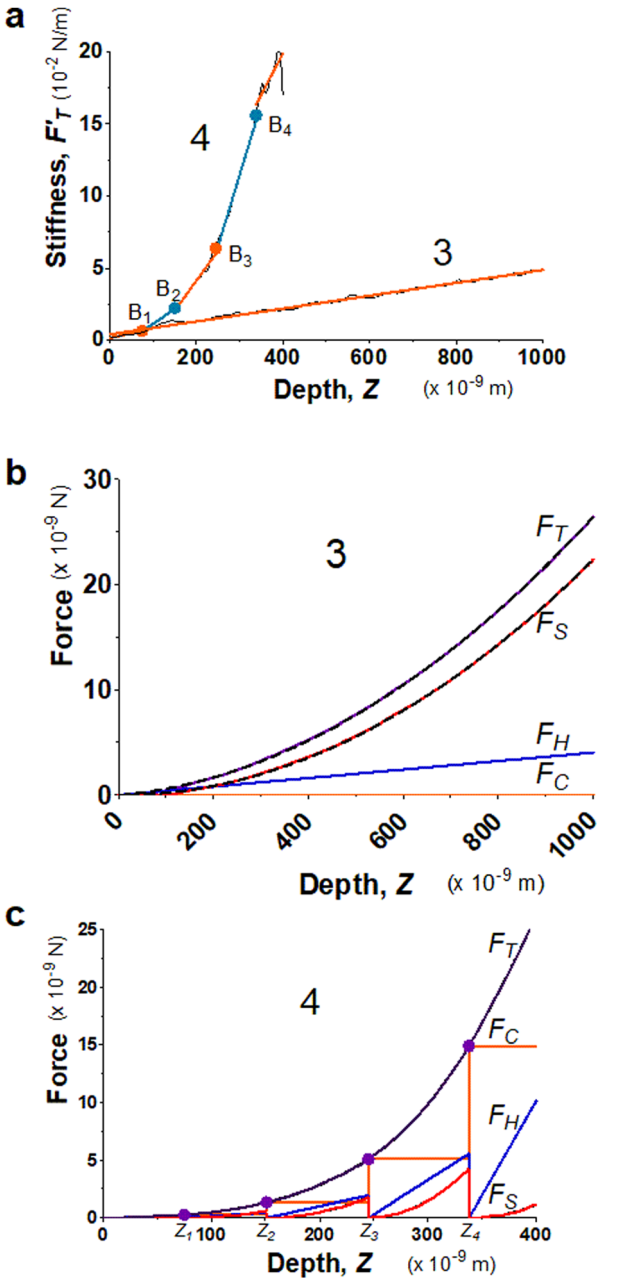

Fig. 3 Elastic behaviors of two 4 day-old seedling roots from *A. thaliana* (System 3 and 4) under AFM indentations. (a) The stiffness–depth curves of the two root systems, and labeled by 3 and 4, respectively. The black solid line presents F_T-derived stiffness curves, and the linear fitted segments are indicated by alternating colors, orange and light blue. The Z-coordinates of breaking points for System 4 are Z_1 = 74.8, Z_2 = 151, Z_3 = 245 and Z_4 = 338 nm. The single R_S of System 3 equals 44.7 kPa, and for the sequential segments of System 4, $R_{S,1}$ = 67.2, $R_{S,2}$ = 209, $R_{S,3}$ = 417, $R_{S,4}$ = 989, and $R_{S,5}$ = 570 kPa. (b) Application of trimechanic-3PCS model to System 3. The parameters of trimechanic-3PCS quadruplet are shown in Table 2. (c) Application of trimechanic-3PCS model to System 4. The trimechanic-3PCS quadruplets for the five depth-zones are listed in Table 2. All the plots of F_T as well as F_C, F_H and F_S against Z are respectively presented by magenta, orange, blue and red lines. The fitting results are delineated by black dashed lines.

45.5 kPa respectively from the trimechanic-3PCS model and AtomicJ-pyramid for System 3. On the contrary, for System 4,

Table 2 The results of 3PCS quadruplet parameters for plant seedling roots

	System 3	System 4				
Zone index	1	1	2	3	4	5
ΔZ (nm)	1000	74.8	76.0	94.2	92.9	62.0
k_C (mN m^{-1})	0.00	0.00	3.64	14.3	55.1	241
k_T (mN m^{-1})	27.2	3.93	13.9	39.4	105	182
r_S	0.85	0.63	0.57	0.48	0.43	0.10
$\hat{E}$ (kPa)	45.2	67.5	211	403	984	611

the discrepancy becomes severe between the two models (Fig. S2d, ESI†). As mentioned previously, the F_T-derived stiffness of this system cannot be modeled as one single linear segment, *i.e.* uniform elasticity. Nevertheless, the trimechanic-3PCS model reports the $\hat{E}$ values, ranging from 67.5 to 611 kPa, to describe the elasticity variation with depth. Results for the full plant datasets can be found graphically in Fig. S3c and d (ESI†).

For a live tissue of plant root, the magnitude and variation rate of stiffness with indented depth reflect the change of elastic properties through the thickness of the cell wall. In particular, the tip-shape nanomechanics (F_S) was found to exert a lower impact on the total response in deeper depth-zones, reflected by a decreased value of r_S or F_S weight. Such deeper indentations render the surface of the material so stiff that the surface hardly deforms itself to accord with the tip shape. One should not naively attribute the discrepancy between the results of trimechanic-3PCS and AtomicJ-pyramid models solely to the different choice of the contact point. We show in Fig. S1a (ESI†) that even the contact points determined by the two approaches are close, one still obtains incomparable results.

Conclusions

Trimechanic theory is a straightforward outcome of extending the applicability of the Sneddon's pyramid model to the study of elastic heterogeneity. The three force/nanomechanics components, F_C, F_H and F_S, carry information of the impact of hitherto indentation on the material. Analogous to the coordinates of a point in the three-dimensional space, (k_C, k_H, k_S) can be referred to the coordinates of an elastic response in the nanomechanical space, which is spanned by the three modes of nanomechanics. Excellent fittings of F_T curves by the trimechanic theory indicate that the best use of the Sneddon's model should be restricted to the F_S component instead of the total force F_T, and that the Hookean nanomechanics is substantial in the response. The stiffness-based approach to identification of same elasticity can extend to Hertz-spherical-tip model or a model whose force–depth relation follows the power law (a preliminary result for Hertz model is shown in Fig. S4, ESI†). The 3PCS quadruplet [ΔZ, k_C, k_T, r_S] contains all information on characterizing the elastic response of material, from which the modeled forces along the indentation depth can be reconstructed: $F_T = (k_C + k_T)\cdot\Delta Z$, k_T itself is the extrinsic stiffness, and $\hat{E}$ can be derived from k_T and r_S. Moreover, the combinatory ratio of r_S and r_H alludes to bonding deformability of the

composite material. With a nano-sized tip, AFM indentation combined with the trimechanic-3PCS framework provides us a technique to measure the structural stiffness of soft biomaterials, and to quantify the difference of restoring mechanisms from a variety of material conditions. The extended elasticity parameters bring a larger breadth on data comparison than one single parameter, leading to a finer differentiation between elastic properties of materials.

Author contributions

S. W. C. and J. L. P. conceived the study. S. W. C. developed the theory and performed the computational analysis. J. M. T. designed and made the gels and performed their indentation. H. K. and C. G. designed and performed indentation on plant roots. S. W. C. and J. L. P. wrote the manuscript with the contributions of all authors.

Conflicts of interest

There are no conflicts to declare.

Acknowledgements

IBS acknowledges integration into the Interdisciplinary Research Institute of Grenoble (IRIG, CEA). This work acknowledges the AFM platform at the IBS. Dr Anne-Emmanuelle Foucher (IBS, group EPIGEN) is acknowledged for her contribution to polyacrylamide gels. Dr Thierry Desnos (CEA, BIAM) is acknowledged for his contribution to the *Arabidopsis thaliana* project. Prof. Felix Rico (INSERM, Marseille) and Alessandro Podesta (Univ. Milano) are acknowledged for their useful discussions. Acknowledgment to the ANR project BioPhyt-18-CE20-0023-03 and the support of the European Union's Horizon 2020 research and innovation programme under the Marie Skłodowska-Curie grant agreement No. 812772, Project Phys2BioMed.

Notes and references

1 J. H. Wang and B. P. Thampatty, *Biomech. Model. Mechanobiol.*, 2006, **5**, 1–16.
2 V. Vogel, *Annu. Rev. Physiol.*, 2018, **80**, 353–387.
3 J. F. Stoltz and X. Wang, *Biorheology*, 2002, **39**, 5–10.
4 R. M. Hochmuth, *J. Biomech.*, 2000, **33**, 15–22.
5 H. Zhang and K. K. Liu, *J. R. Soc., Interface*, 2008, **5**, 671–690.
6 O. Otto, P. Rosendahl, A. Mietke, S. Golfier, C. Herold, D. Klaue, S. Girardo, S. Pagliara, A. Ekpenyong, A. Jacobi, M. Wobus, N. Topfner, U. F. Keyser, J. Mansfeld, E. Fischer-Friedrich and J. Guck, *Nat. Methods*, 2015, **12**, 199–202.
7 R. Prevedel, A. Diz-Munoz, G. Ruocco and G. Antonacci, *Nat. Methods*, 2019, **16**, 969–977.
8 M. Krieg, G. Flaschner, D. Alsteens, B. M. Gaub, W. H. Roos, G. J. L. Wuite, H. E. Gaub, C. Gerber, Y. F. Dufrene and D. J. Muller, *Nat. Rev. Phys.*, 2019, **1**, 41–57.
9 M. Lekka, P. Laidler, D. Gil, J. Lekki, Z. Stachura and A. Z. Hrynkiewicz, *Eur. Biophys. J.*, 1999, **28**, 312–316.
10 I. Sokolov, in *Cancer Nanotechnology*, ed. H. S. Nalwa and T. Webster, American Scientific Publishers, 2007, ch. 1, pp. 1–17.
11 S. Kumar and V. M. Weaver, *Cancer Metastasis Rev.*, 2009, **28**, 113–127.
12 M. Lekka, K. Pogoda, J. Gostek, O. Klymenko, S. Prauzner-Bechcicki, J. Wiltowska-Zuber, J. Jaczewska, J. Lekki and Z. Stachura, *Micron*, 2012, **43**, 1259–1266.
13 M. Plodinec, M. Loparic, C. A. Monnier, E. C. Obermann, R. Zanetti-Dallenbach, P. Oertle, J. T. Hyotyla, U. Aebi, M. Bentires-Alj, R. Y. Lim and C. A. Schoenenberger, *Nat. Nanotechnol.*, 2012, **7**, 757–765.
14 M. Radmacher, M. Fritz, C. M. Kacher, J. P. Cleveland and P. K. Hansma, *Biophys. J.*, 1996, **70**, 556–567.
15 M. Radmacher, *Methods Cell Biol.*, 2007, **83**, 347–372.
16 P. Carl and H. Schillers, *Pflugers Archiv.*, 2008, **457**, 551–559.
17 H. Hertz, *C. Vermischte Abhandlungen.*, 1882, pp. 449–464.
18 I. N. Sneddon, *Int. J. Eng. Sci.*, 1965, **3**, 47–57.
19 F. Rico, P. Roca-Cusachs, N. Gavara, R. Farre, M. Rotger and D. Navajas, *Phys. Rev. E: Stat., Nonlinear, Soft Matter Phys.*, 2005, **72**, 021914.
20 J. Zemla, J. Bobrowska, A. Kubiak, T. Zielinski, J. Pabijan, K. Pogoda, P. Bobrowski and M. Lekka, *Eur. Biophys. J.*, 2020, **49**, 485–495.
21 S. Chiodini, S. Ruiz-Rincon, P. D. Garcia, S. Martin, K. Kettelhoit, I. Armenia, D. B. Werz and P. Cea, *Small*, 2020, **16**, e2000269.
22 S. V. Kontomaris and A. Malamou, *Eur. J. Phys.*, 2022, **43**, 015010.
23 G. Persch, C. Born and B. Utesch, *Microelectron. Eng.*, 1994, **24**, 113–121.
24 E. K. Dimitriadis, F. Horkay, J. Maresca, B. Kachar and R. S. Chadwick, *Biophys. J.*, 2002, **82**, 2798–2810.
25 N. Gavara and R. S. Chadwick, *Nat. Nanotechnol.*, 2012, **7**, 733–736.
26 P. D. Garcia and R. Garcia, *Biophys. J.*, 2018, **114**, 2923–2932.
27 K. L. Johnson, K. Kendall and A. D. Roberts, *Proc. R. Soc. London, Ser. A*, 1971, **324**, 301–313.
28 B. V. Derjaguin, V. M. Muller and Y. P. Toporov, *J. Colloid Interface Sci.*, 1975, **53**, 314–326.
29 S. Kasas, X. Wang, H. Hirling, R. Marsault, B. Huni, A. Yersin, R. Regazzi, G. Grenningloh, B. Riederer, L. Forro, G. Dietler and S. Catsicas, *Cell Motil. Cytoskeleton*, 2005, **62**, 124–132.
30 S. Digiuni, A. Berne-Dedieu, C. Martinez-Torres, J. Szecsi, M. Bendahmane, A. Arneodo and F. Argoul, *Biophys. J.*, 2015, **108**, 2235–2248.
31 D. C. Lin, D. I. Shreiber, E. K. Dimitriadis and F. Horkay, *Biomech. Model. Mechanobiol.*, 2009, **8**, 345–358.
32 A. J. Engler, S. Sen, H. L. Sweeney and D. E. Discher, *Cell*, 2006, **126**, 677–689.
33 G. Kaushik, A. Fuhrmann, A. Cammarato and A. J. Engler, *Biophys. J.*, 2011, **101**, 2629–2637.
34 B. L. Doss, K. Rahmani Eliato, K. H. Lin and R. Ros, *Soft Matter*, 2019, **15**, 1776–1784.

35 V. G. Gisbert and R. Garcia, *ACS Nano*, 2021, **15**, 20574–20581.
36 J. Boussinesq, *Application des potentiels à l'étude de l'équilibre et du mouvement des solides élastiques, avec des notes étendues sur divers points de physique mathématique et d'analyse*, Gauthier-Villars Imprimeur-Libraire, Paris, 1885.
37 C. Roduit, S. Sekatski, G. Dietler, S. Catsicas, F. Lafont and S. Kasas, *Biophys. J.*, 2009, **97**, 674–677.
38 A. C. Dumitru, M. A. Poncin, L. Conrard, Y. F. Dufrene, D. Tyteca and D. Alsteens, *Nanoscale Horiz.*, 2018, **3**, 293–304.
39 S. Janel, M. Popoff, N. Barois, E. Werkmeister, S. Divoux, F. Perez and F. Lafont, *Nanoscale*, 2019, **11**, 10320–10328.
40 H. Schillers, C. Rianna, J. Schäpe, T. Luque, H. Doschke, M. Wälte, J. J. Uriarte, N. Campillo, G. P. Michanetzis, J. Bobrowska, A. Dumitru, E. T. Herruzo, S. Bovio, P. Parot, M. Galluzzi, A. Podestà, L. Puricelli, S. Scheuring, Y. Missirlis, R. Garcia, M. Odorico, J. M. Teulon, F. Lafont, M. Lekka, F. Rico, A. Rigato, J.-L. Pellequer, H. Oberleithner, D. Navajas and M. Radmacher, *Sci. Rep.*, 2017, **7**, 5117.
41 J. R. Tse and A. J. Engler, *Current Protocols in Cell Biology*, 2010, ch. 10, pp. 10–16.
42 C. Balzergue, T. Dartevelle, C. Godon, E. Laugier, C. Meisrimler, J.-M. Teulon, A. Creff, M. Bissler, C. Brouchoud, A. Hagège, J. Müller, S. Chiarenza, H. Javot, N. Becuwe-Linka, P. David, B. Péret, E. Delannoy, M.-C. Thibaud, J. Armengaud, S. Abel, J.-L. Pellequer, L. Nussaume and T. Desnos, *Nat. Commun.*, 2017, **8**, 15300.
43 H. Kaur, C. Godon, J.-M. Teulon, T. Desnos and J.-L. Pellequer, in *Mechanics of Cells and Tissues in Diseases*, ed. M. Lekka, D. Navajas, M. Radmacher and A. Podestà, Walter de Gruyter GmbH, Berlin/Boston, 2023, vol. 2, pp. 125–138.
44 T. Murashige and F. Skoog, *Physiol. Plant.*, 1962, **15**, 473–497.
45 D. P. Blattler, F. Garner, K. van Slyke and A. Bradley, *J. Chromatogr.*, 1972, **64**, 147–155.
46 A. Rath, F. Cunningham and C. M. Deber, *Proc. Natl. Acad. Sci. U. S. A.*, 2013, **110**, 15668–15673.
47 P. Hermanowicz, M. Sarna, K. Burda and H. Gabrys, *Rev. Sci. Instrum.*, 2014, **85**, 063703.
48 P. Albersheim, A. Darvill, K. Roberts, R. Sederoff and A. Staehelin, *Plant cell walls. From chemitry to biology*, Garland Science, Taylor & Francis Group, LLC, New York, NY, USA, 2011.
49 D. Gaff and D. Carr, *Aust. J. Biol. Sci.*, 1961, **14**, 299–311.
50 S. Tsugawa, Y. Yamasaki, S. Horiguchi, T. Zhang, T. Muto, Y. Nakaso, K. Ito, R. Takebayashi, K. Okano, E. Akita, R. Yasukuni, T. Demura, T. Mimura, K. Kawaguchi and Y. Hosokawa, *Sci. Rep.*, 2022, **12**, 13044.
51 P. Derbyshire, K. Findlay, M. C. McCann and K. Roberts, *J. Exp. Bot.*, 2007, **58**, 2079–2089.

